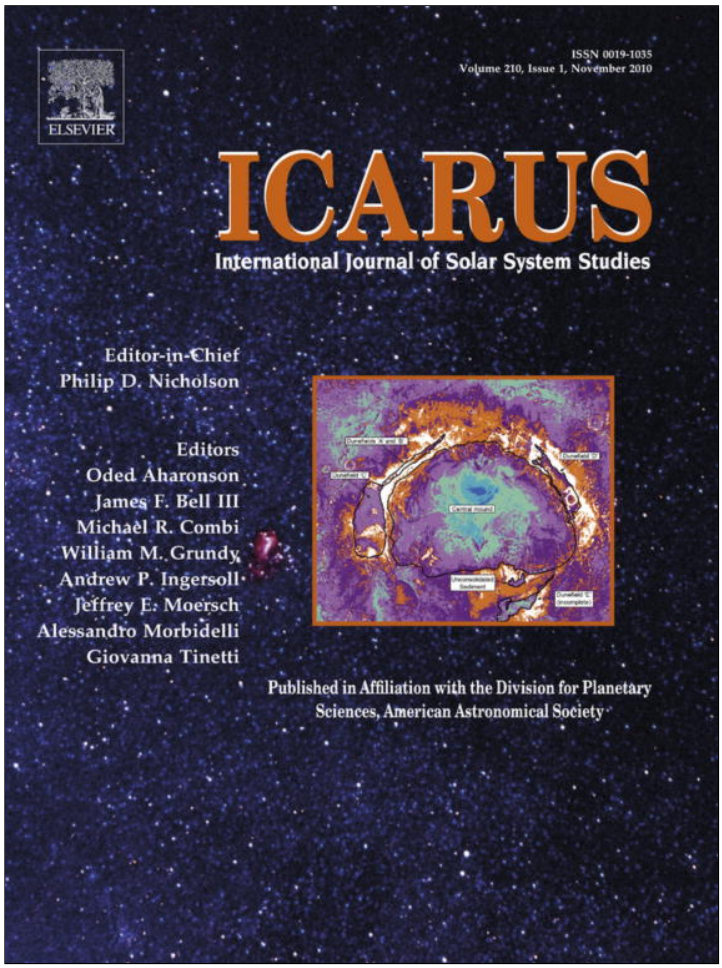

Icarus 210 (2010) 396–410

Contents lists available at ScienceDirect

Icarus

journal homepage: www.elsevier.com/locate/icarus

The effects of strain localization on the formation of Ganymede's grooved terrain

Michael T. Bland [a,*], William B. McKinnon [a], Adam P. Showman [b]

[a] Department of Earth and Planetary Sciences and McDonnell Center for Space Sciences, Washington University, Saint Louis, MO 63130, United States
[b] Department of Planetary Science, Lunar and Planetary Laboratory, University of Arizona, Tucson, AZ 85721, United States

ARTICLE INFO

Article history:
Received 2 December 2009
Revised 3 June 2010
Accepted 8 June 2010
Available online 15 June 2010

Keywords:
Ganymede
Tectonics
Satellites, Surfaces
Jupiter, Satellites
Ices

ABSTRACT

We investigate the effects of strain localization on the formation of Ganymede's grooved terrain by numerically modeling the extension of an ice lithosphere in which the yield strength of the ice decreases as the magnitude of the plastic strain increases. We do this to more realistically model fault strength, which is expected to vary with slip during initial fault development. We find that the inclusion of strain weakening leads to the formation of periodic structures with amplitudes of 200–500 m, consistent with the observed amplitudes of Ganymede's large-scale grooves. The morphology of the deformation that results from extension depends both on the thermal gradient, which sets the lithospheric thickness, and on the rate at which the yield strength of the ice decreases with increasing plastic strain. Slow weakening with strain leads to low-amplitude, periodic structures, whereas moderate to rapid weakening with strain leads to large-amplitude, non-periodic structures. The combined influence of the thermal gradient and the weakening rate leads to the formation of complex surface deformation and may help explain the variety of surface morphologies observed within the grooved terrain.

1. Introduction

Ganymede's surface consists of broad regions of ancient, heavily cratered terrain that are disrupted by innumerable swaths of young (~2 Ga) (Zahnle et al., 2003), tectonically and possibly cryovolcanically modified terrain (e.g., Smith et al., 1979a,b; Pappalardo et al., 1998, 2004; Schenk et al., 2001). The tectonic deformation within this young terrain typically has a common morphology, termed grooved terrain, that consists of sets of quasi-parallel, periodically spaced ridges-and-troughs (Fig. 1). Individual troughs are often continuous along strike for 100–1000 km and groove sets are typically 10–100 km in width. A distinct feature of Ganymede's grooved terrain is the periodic spacing of ridges within each groove set. Fourier analysis indicates that the dominant wavelength of groove spacing within each set ranges from 3 to 17 km, varying from one groove set to another (Grimm and Squyres, 1985), with prominent shorter wavelengths apparent in sufficiently high-resolution images (Patel et al., 1999). Grooves typically have peak-to-trough amplitudes of 200–500 m (Squyres, 1981; Giese et al., 1998; Pappalardo et al., 1998) and appear to have shallow slopes with root mean squared values of ~5° (Squyres, 1981). While Ganymede's grooves tend to share these general characteristics, the tectonic deformation within the grooved terrain is complex (Fig. 1), and groove swaths often include a variety of surface morphologies including undulating ridges-and-troughs, horst-and-graben-like structures, and tilt-block normal faulting (Pappalardo et al., 1998, 2004).

The grooved terrain likely formed during extension of Ganymede's ice lithosphere (see Pappalardo et al., 2004 and references therein), possibly during an epoch of global satellite expansion caused by differentiation (e.g., Squyres, 1980; Mueller and McKinnon, 1988), or melting during resonance passage (Showman et al., 1997; Bland et al., 2009). The most prominent formation mechanism for the grooved terrain is unstable extension of Ganymede's ice lithosphere (Pappalardo et al., 1998; Collins et al., 1998b; Dombard and McKinnon, 2001; Bland and Showman, 2007). While stable extension results in uniform thinning of the lithosphere, unstable extension results in the amplification of small perturbations in lithospheric thickness (e.g., due to preexisting topography or heat flow variations). Perturbations grow exponentially as extension occurs, with the growth rate of one perturbation wavelength (nominally 3–4 times the lithospheric thickness, but dependent on several factors) exceeding the others (Fletcher and Hallet, 1983; Schmalholz et al., 2008). Typically, the fastest-growing wavelength dominates the final surface deformation. At small strains, the morphology produced by unstable extension consists of periodically spaced, undulating pinch-and-swell structures analogous to lithospheric-scale boudinage (Fletcher and Hallet, 1983).

The recognition of unstable extension's importance as a formation mechanism for Ganymede's grooves has occurred haltingly over the past three decades. Shortly after the Voyager spacecraft first observed the grooved terrain, Fink and Fletcher (1981) used a then-unpublished model for Basin and Range formation via

* Corresponding author. Fax: +1 314 935 7361.
E-mail address: mbland@levee.wustl.edu (M.T. Bland).

0019-1035/$ - see front matter © 2010 Elsevier Inc. All rights reserved.
doi:10.1016/j.icarus.2010.06.008

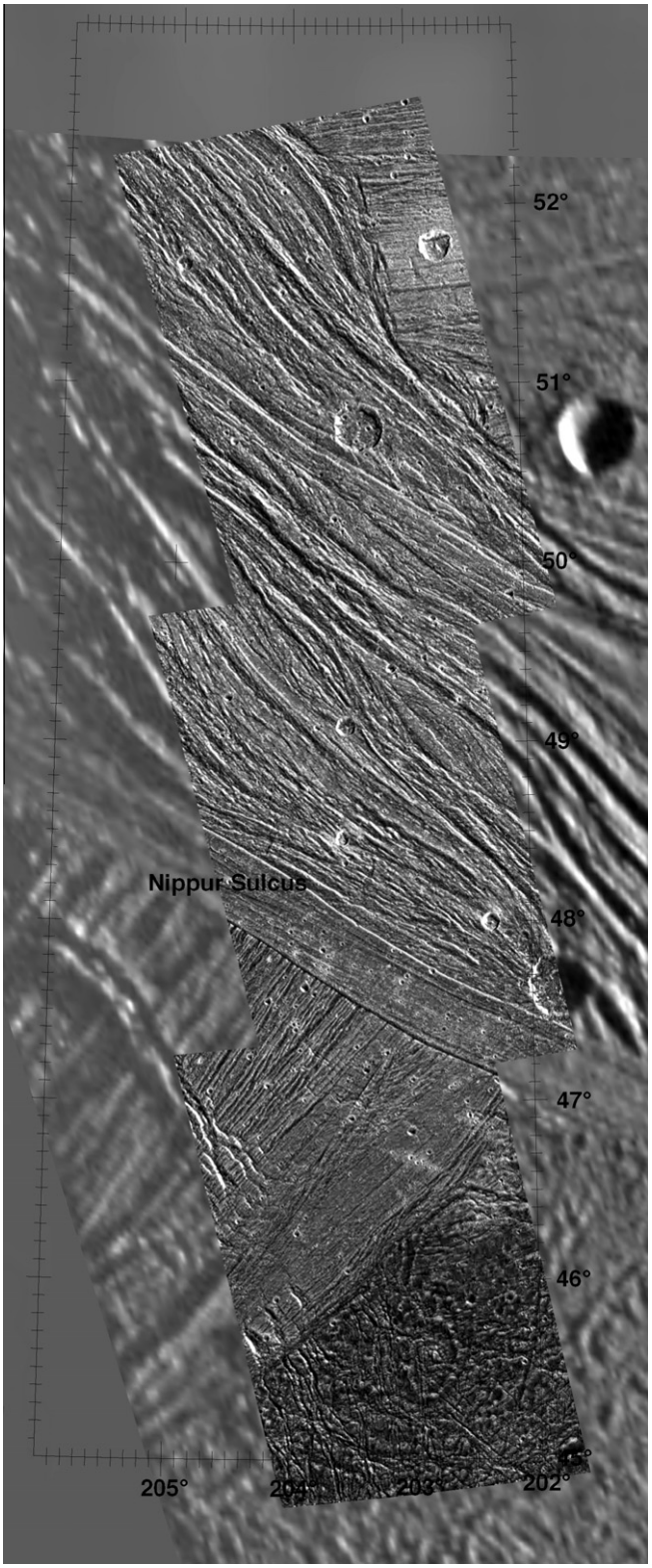

Fig. 1. Overlay of two Galileo images (from orbits G2 and G8) showing multiple groove swaths with different morphologies near Nippur Sulcus (centered at 48°N, 204°W). The ancient, heavily cratered terrain of Marius Regio appears at the bottom of the image. Orthographic projection from Schenk (2010).

unstable extension to suggest that the periodicity of the structures could be used to infer Ganymede's lithospheric thickness. A few years later Golombek and Banerdt (1986) used the same approach to infer that thermal gradients of 4.5–20 K km^{-1} were present at the time of groove formation. Subsequently, Herrick and Stevenson (1990) actually applied the full Fletcher and Hallet (1983) model to an ice lithosphere and found that the topographic growth rates were too small to explain the amplitudes of Ganymede's grooves. In their analysis, the fundamental problem that prevented large growth rates was the insufficient strength contrast between the brittle lithosphere and the underlying ductile ice, which was thought to deform primarily by dislocation creep. Herrick and Stevenson (1990) were thus forced to conclude that unstable extension could not explain Ganymede's grooves (except possibly at polar latitudes).

Since the Herrick and Stevenson (1990) analysis, however, additional deformation mechanisms for ice-I (grain-boundary-sliding (GBS) and basal slip) with lower power-law exponents have been recognized (Goldsby and Kohlstedt, 1997, 2001). The lower power-law exponent (e.g., $n = 1.8$ for GBS) results in lower effective viscosities for GBS than for dislocation creep ($n = 4$), and increases the strength contrast between the strong, brittle ice lithosphere and the ductile ice at depth. Using these newly found flow mechanisms, and arguing for colder lithospheres due to a dimmer, early Sun, Dombard and McKinnon (1996, 2001) revisited the Herrick and Stevenson (1990) investigation and found significantly increased instability growth rates. When extrapolated to large strains ($\gtrsim 10\%$), geological evidence for which became apparent in Galileo images (Collins et al., 1998b), these growth rates would result in periodic structures with crest to trough amplitudes of 500 m or more assuming a 10-m initial perturbation and high thermal gradients (20–40 K km^{-1}) (Dombard and McKinnon, 2001). These large growth rates led them to conclude that the extensional necking model of groove formation *was* consistent with structures observed in Ganymede's grooved terrain. With the success of this model and the addition of high resolution images that supported the extensional necking mechanism (e.g., Pappalardo et al., 1998; Collins et al., 1998b), unstable extension became the defacto model for groove formation.

Despite the success of the Dombard and McKinnon (2001) model, a number of questions regarding groove formation could not be addressed by their analytical approach, which required extrapolation from growth rates determined at infinitesimal strains to large-amplitude topography produced at large local strain ($\sim$10% or more (Collins et al., 1998b)). Zuber and Parmentier (1996) showed that, in compression, instability growth rates begin to decrease as strains become large (depending on initial amplitude), limiting the total amplitude of the deformation produced. Additionally, because each Fourier component is examined individually via a perturbation approach, analytical models do not examine the interaction between wavelengths in an initial surface consisting of random topography once slopes or amplitudes are no longer small (compared to layer thickness). Thus, whether extensional necking can "select" a single dominant wavelength from random initial topography was not entirely clear (though see Fletcher, 1995). We stress, however, that the mere existence of regular arrays of grooves on Ganymede strongly implies selective amplification of linearly independent wavelengths.

To address these question Bland and Showman (2007) used finite-element modeling to examine the formation of groove-like features via unstable extension at large strains and constant yield strength (i.e., strength was not a function of strain or strain rate; see below). Their investigation showed that, while extensional necking successfully selected and amplified a single topographic wavelength, the amplitude of the deformation was too small to be consistent with Ganymede's grooves. Maximum deformation amplitudes were no greater than $\sim$70 m after 30% strain (assuming a 10 m initial perturbation), more than a factor of five less than amplitudes observed on Ganymede (Bland and Showman, 2007). The small-amplitudes of the finite-strain numerical models

relative to the infinitesimal strain models of Dombard and McKinnon (2001) result from both lower initial growth rates and a decrease in growth rates as strain becomes large (Bland and Showman, 2007). The low-amplitude deformation produced by these numerical models of groove formation suggest that ductile necking alone, with plasticity governed by strain independent yield strength, may be insufficient to produce large-amplitude topography. One issue is the low initial growth rate, which we return to at the conclusion of the paper. But it is also almost certain that an additional mechanism or mechanisms act to localize strain during extension (e.g., Montési and Collins, 2005), which is the central subject of this paper.

2. Strain localization

In many natural systems strain does not accumulate homogeneously throughout a given medium but is localized into narrow bands of deformation. In geologic systems such localization occurs at nearly every length scale (see Regenauer-Lieb and Yuen (2003) for a review). Shear localization begins at grain and sub-grain boundaries within rocks via cracking, dynamic recrystallization, and the formation of lattice preferred crystal orientations (e.g., Jin et al., 1998). Such small-scale localization eventually manifests itself at outcrop and planetary scales (Regenauer-Lieb and Yuen, 2003), resulting in large shear zones and plate boundaries (e.g., Bercovici, 1995; Tackley, 1998).

Strain localization can occur via a number of mechanisms (e.g., Montési and Zuber, 2002). Viscous strain softening due to shear heating (e.g., Brun and Cobbold, 1980; Fleitout and Froidevaux, 1980; Poirier, 1980; Bercovici, 1996; Gerbault, 2000) or grain size reduction (Jin et al., 1998; Braun et al., 1999) contributes to localization. Numerical models of terrestrial extension indicate that the inclusion of viscous strain softening allows increased deformation amplitudes relative to simulations that do not include softening (Frederiksen and Braun, 2001). Strain localization in the brittle regime may play an equal role in localizing strain (Huismans and Beaumont, 2003). In the brittle regime, strain weakening occurs via a decrease in the cohesive strength and/or internal friction of a material after the onset of yielding. Weakening can occur in several ways. Along a discrete fault, gouge formation can lead to decreased cohesion or friction, weakening the fault and permitting increased deformation (e.g., Lachenbruch and Sass, 1980; Zoback et al., 1987). Additionally, the introduction of pore fluid can relieve normal stresses along faults, decreasing the shear required for slip to occur (e.g., Lachenbruch and Sass, 1980). Weakening can also occur through the development of damage within a material. In non-granular material the accommodation of stress through plastic deformation generates voids and microfractures (i.e., damage). As plastic strain accumulates, these microfractures and voids coalesce into new macro-scale cracks where slip can occur (Lemaître, 1992). These microfractures, voids, and cracks decrease the strength of the material, permitting failure to occur at a lower yield strength. However, in porous granular material the development of microfractures can result in distributed cataclastic flow that decreases material porosity and leads to strain hardening rather than weakening (e.g., Menéndez et al., 1996; Wong et al., 1997). Thus the relationship between damage and weakening in a material is non-trivial: if damage leads to a loss of cohesion the material will experience strain weakening, if damage leads to cataclasis *and* a loss of porosity the material will experience strain harding (locking).

Many numerical models of tectonic deformation in terrestrial environments account for strain weakening by decreasing the effective yield strength of the material as the magnitude of the plastic strain increases. Because the processes that lead to strain localization generally occur at temporal and spatial scales much smaller than those of the tectonic deformation being modeled (see Regenauer-Lieb and Yuen, 2003), localization is often parameterized by a reduction in the material's angle of internal friction (e.g., Beaumont et al., 1996; Huismans and Beaumont, 2002, 2003; Huismans et al., 2005), cohesive strength (e.g., Buck and Poliakov, 1998; Poliakov and Buck, 1998; Lavier et al., 1999, 2000; Buck et al., 2003), or both (e.g., Buck et al., 2003; Moresi and Mühlhaus, 2006; Gessner et al., 2007; Delescluse et al., 2008). Such models seek to incorporate the premise that failure of a material depends, in part, on whether that material has failed previously (i.e., on the material's strain history), without necessarily invoking a specific mechanism responsible for weakening (e.g., gouge formation, etc.). In each case, weakening in the brittle regime results in strain localization that allows complex, large-amplitude deformation.

The assumption made by these models, that strain weakening occurs in highly-strained rocks, is well justified by experimental work and field observations. However, the processes that might lead to strain weakening in an ice lithosphere are somewhat less obvious. In the viscous regime, weakening may result from grain size reduction during strain if it allows a transition from dislocation creep to grain-size-sensitive mechanisms (Barr and McKinnon, 2007). Additionally, shear heating of ice would result in decreases in viscosity that could lead to significant strain localization. Models of the dynamics of large ice masses under terrestrial conditions have shown that, under some conditions, shear heating can become unstable, leading to a runaway decrease in viscosity that localizes strain (Yuen and Schubert, 1979; cf. Kaus and Podladchikov, 2006). Strain weakening in the brittle regime is more difficult to explain. Because liquid water is denser than the surrounding ice shell any melt formed during deformation would quickly percolate away or refreeze as the ice shell cooled. Substantial pore-fluid pressure is therefore likely to be negligible in an ice lithosphere (although transient, frictionally-generated water is not out of the question). Additionally, on Earth the formation of fault gouge generally involves not just the physical destruction of the faulted rock but also hydration reactions that form abundant, low-friction, clay minerals, which then permit weakening of the fault (e.g., Wu, 1978; Wang et al., 1980; Rutter et al., 1986). Clearly, the formation of clay minerals cannot occur within a pure ice lithosphere. A more promising mechanism of brittle weakening of ice is the production of damage within the ice lithosphere. As strain increases, the formation of randomly oriented microfractures and voids may permit subsequent failure at stress levels lower than those required to create the initial microfractures, resulting in the loss of cohesive strength.

Indeed, the accumulation of damage during lithospheric deformation seems unavoidable. Unfortunately, experimental data on the brittle behavior of ice at temperatures relevant to Ganymede (70–120 K at the time of groove formation (Dombard and McKinnon, 2001)) is currently limited (Beeman et al. (1988) is the exception) and data on the influence of strain history on the yield strength of ice at these temperatures is non-existent. Ice at very low temperatures generally behaves like a weak rock however (e.g., Beeman et al., 1988; Durham and Stern, 2001), thus strain induced weakening of ice appears a likely process. One would, in fact, be hard-pressed to argue the converse on physical grounds. Furthermore, we emphasize that while rheological data may be sparse, there is abundant morphological evidence for strain localization, faulting and fracturing both within Ganymede's grooved terrains (e.g., Pappalardo et al., 1998; Collins et al., 1998b) and within ice lithospheres in general (see Collins et al. (2010) for a review).

In this paper we explore the effects of strain weakening in the brittle regime on an ice lithosphere undergoing extension. In Section 3 we describe the numerical model and our implementation of strain weakening. In Section 4 we describe the results of

simulations that include strain weakening, compare them to previous simulations that did not include weakening, and examine whether the morphology of deformation produced by these simulations approximates the deformation found in Ganymede's grooved terrain. In Section 5 we summarize our findings, offer some perspectives on the application of numerical models to Ganymede's tectonic evolution, and describe future data and modeling necessary for further progress.

3. Modeling the formation of grooved terrain

We use the two-dimensional, Lagrangian, finite-element model Tekton (v2.3) (Melosh and Raefsky, 1980) to simulate the extension of an ice lithosphere. Our model domains were 40 km long and 24 km deep: long enough to permit several wavelengths of deformation across their surface and deep enough to prevent the bottom boundary from influencing the surface deformation. The horizontal resolution of the finite-element mesh was 167 m. The vertical resolution varied from 167 m in the top 10 km to 500 m in the bottom 5 km of the mesh, giving a total of 240 × 97 quadrilateral elements. A small-amplitude (10 m), sinusoidal topographic perturbation was introduced to the top surface to allow deformation to initiate. The perturbation wavelength was chosen so as to maximize the topographic amplification for a give thermal gradient. That is, the perturbation uses the "dominant wavelength" for growth (e.g., ~6 km for dT/dz = 10 K km^{-1}) (see Bland and Showman, 2007).

Extension of the domain was produced by assigning a fixed horizontal boundary condition on the left-hand side of the domain and a constant horizontal velocity boundary condition on the right-hand side. Both boundaries were free-slip in the vertical. The bottom boundary was fixed in the vertical direction and free-slip in the horizontal. Nominally we imposed 20% extension of the domain (with no remeshing), though we also investigated strains up to 30%. Our simulated strains are consistent with the strain measured across moderate to high-relief grooves (~15% to >100%) (Collins, 2008) and deformed craters (0% to >100%) (Pappalardo and Collins, 2005). As with the age of the groove terrain, the time span over which individual groove swaths formed on Ganymede is largely unconstrained. However, Bland and Showman (2007) showed that groove formation depends only weakly on the strain rate for values between 10^{-13} and 10^{-15} s^{-1}. Thus, we use a strain rate of 10^{-13} s^{-1} (30% extension in 10^5 yrs), with a time step of 1 yr, to minimize required computation time (the smallest time step is set by the Maxwell time of the least viscous element). Note that extension at a constant velocity is not identical to extension at a constant strain rate (i.e., as the domain extends strain rate decreases modestly). We impose a constant gravitational acceleration of 1.4 m s^{-2} and initialize the stresses by allowing the mesh below the lithosphere to (mostly) relax to a hydrostatic state before extension begins.

We assume a surface temperature of 70 K consistent with Ganymede's polar regions and previous modeling (Dombard and McKinnon, 2001; Bland and Showman, 2007) and, in the nominal model, impose a thermal gradient of 10 K km^{-1}. Model results are somewhat sensitive to the assumed surface temperature, with resulting topographic amplitudes decreasing as temperature increases. The consistent use of a 70 K surface temperature reduces the number of free parameters involved in this study, however, and allows us to test our models under the most favorable conditions plausible for Ganymede. For numerical stability we limit the maximum temperature (of deep ice) to 200 K, at which point the domain becomes isothermal. Tekton does not explicitly include thermodynamics so isotherms are passively advected along with the elements. Thus, extensional thinning forces isotherms closer together and the imposed thermal gradient increases modestly throughout the simulation. This effect has negligible influence on the results described here and is discussed in greater detail in Bland and Showman (2007). More important, however, is that we do not track dissipation during model calculations, and so are not simulating strain softening and possible localization due to shear heating (e.g., Kaus and Podladchikov, 2006).

3.1. Rheology

The model includes the elastic, viscous, and plastic behavior of ice. Table 1 shows the properties of ice assumed in our simulations. The viscous behavior of ice is modeled using a composite power-law rheology with the form

$$\dot{\varepsilon}_{visco} = \dot{\varepsilon}_A + \dot{\varepsilon}_B + \dot{\varepsilon}_C + \{1/\dot{\varepsilon}_{GBS} + 1/\dot{\varepsilon}_{BS}\}^{-1}, \quad (1)$$

where subscripts A, B, C, GBS, and BS refer to dislocation creep A, B, and C; grain-boundary-sliding; and basal slip. Each of these mechanisms has a temperature and stress dependence of the form

$$\dot{\varepsilon}_E = \frac{3^{(n+1)/2}}{2} A (1/d)^m \acute{\sigma}_E^n exp\{-Q/RT\}, \quad (2)$$

where $\dot{\varepsilon}_E$ and $\acute{\sigma}_E$ are the effective strain rate and effective shear stress, respectively, A is a mechanism-dependent constant, d is the grain size, m is the grain size exponent, n is the power-law exponent, Q is the activation energy, R is the gas constant, and T is the absolute temperature. The numerical factor $3^{(n+1)/2}/2$ modifies the experimentally-derived rheological constant A for use in a plane-strain geometry (see Section 4.4 in Ranalli (1995)). Table 2 shows the relevant rheological parameters for each flow mechanism. In all cases we assume a grain size of 1 mm (Barr and McKinnon, 2007).

Plasticity is a continuum approach to modeling brittle behavior that assumes that the lithosphere is pervasively fractured on a scale finer than the element resolution and that the combined behavior of these fractures can be modeled as an addition to the viscous strain rate. We model plastic behavior with a Drucker–Prager yield criterion (which approximates the traditional Mohr–Coulomb criterion but is numerically more tractable because it is smooth) with the form

$$\sqrt{J_2} = \tau_\circ \equiv \beta - \alpha\sigma_m, \quad (3)$$

Table 1
Ice parameters.

Symbol	Parameter	Value
E	Young's modulus[a]	9.3 GPa
v	Poisson ratio[a]	0.325
ρ	Density[b]	980 kg m^{-3}
C	Cohesion[c]	10 MPa
ϕ	Angle of internal friction	30°

[a] Data of Gammon et al. (1983).
[b] Cold ice, slightly impure (dense).
[c] We use a cohesion one order of magnitude larger than that measured by Beeman et al. (1988). See text.

Table 2
Rheological parameters.[a]

Creep regime	Log A (MPa^{-n} m^m s^{-1})	m	n	Q (kJ mole^{-1})
Dislocation creep				
Regime A	11.8	0	4.0	91
Regime B	5.1	0	4.0	61
Regime C	−3.8	0	6.0	39
GBS	−2.4	1.4	1.8	49
BS	7.74	0	2.4	60

[a] Durham and Stern (2001).

where $\tau_\circ$ is the yield strength, J_2 is the second invariant of the stress deviator (which makes $\sqrt{J_2} \equiv \acute{\sigma}_E$), σ_m is mean normal stress (negative in compression), and β and α are related to the material cohesion, C, and angle of internal friction, ϕ, by (Owen and Hinton, 1980)

$$\beta = \frac{6C\cos\phi}{\sqrt{3}(3-\sin\phi)}, \tag{4}$$

and

$$\alpha = \frac{6\sin\phi}{\sqrt{3}(3-\sin\phi)}. \tag{5}$$

The resulting lithospheric strength profile (in terms of effective shear stress) is shown in Fig. 2 for a thermal gradient of 10 K km^{-1} and a strain rate of 10^{-13} s^{-1}. Note that, even in the absence of strain weakening, the dependence on mean stress in Eq. (3) results in local decreases in yield strength as extension occurs and tensile (positive) stresses become large in the near surface (gray line, Fig. 2). As shown in Fig. 2, the brittle–ductile transition (BDT) in our nominal model occurs at a depth of 4.6 km, generally consistent with the region in which plastic deformation is observed to occur (see Fig. 5). The depth to the BDT decreases with increasing thermal gradient and decreasing strain rate (see Fig. 8). We also note that our initial cohesion (Table 1) implies an initially strong ice lithosphere even in extension. We retain this value, which is consistent with Bland and Showman (2007), to facilitate direct comparisons to that work, and to focus on understanding the effects of strain weakening.

When the square root of the second invariant of the deviatoric stress in an element exceeds the yield criterion (which defines the yield surface, τ_{yield}) plastic failure occurs and the strain rate becomes

$$\dot{\varepsilon}_{total} = \dot{\varepsilon}_{elastic} + \dot{\varepsilon}_{visco} + \dot{\varepsilon}_{plastic} \tag{6}$$

where $\dot{\varepsilon}_{elastic}$ is due to the elastic strain. The magnitude of $\dot{\varepsilon}_{plastic}$ is determined with an associated flow rule (i.e., once failure occurs stress returns to the yield surface via a path normal to the surface, see Owen and Hinton, 1980) and depends on the local stress conditions (i.e., the distance outside the yield surface) and the rate at which stress relaxes back to the yield surface.

We utilize a heuristic model of strain weakening in which the yield strength (τ_{yield}) of a given element decreases linearly with increasing plastic strain as

$$\tau_{yield} = \tau_\circ\left[1 - a\left(\frac{e_2^{\frac{1}{2}}}{\epsilon}\right)\right] \tag{7}$$

where $\tau_\circ$ is the unweakened yield strength calculated from Eq. (3), and $e_2^{1/2}$ is the square root of the second invariant of the plastic strain. The parameter a controls the minimum permissible yield strength relative to $\tau_\circ$ (e.g., a = 0.8 corresponds to a minimum τ_{yield} that is 20% of $\tau_\circ$). The value of the saturation strain ϵ controls the rate at which weakening occurs: large values of ϵ result in "slow" weakening with strain; small values of ϵ result in "rapid" weakening with strain. Once the magnitude of the plastic strain $\left(e_2^{\frac{1}{2}}\right)$ in an element exceeds the value of ϵ the ratio $e_2^{\frac{1}{2}}/\epsilon$ is set equal to 1. The model is consistent with the approach of Buck and Poliakov (1998), Gessner et al. (2007), and Delescluse et al. (2008). For numerical stability weakening was not permitted in elements adjacent to the left and right vertical boundary of the domain. Several weakening profiles are shown in Fig. 3.

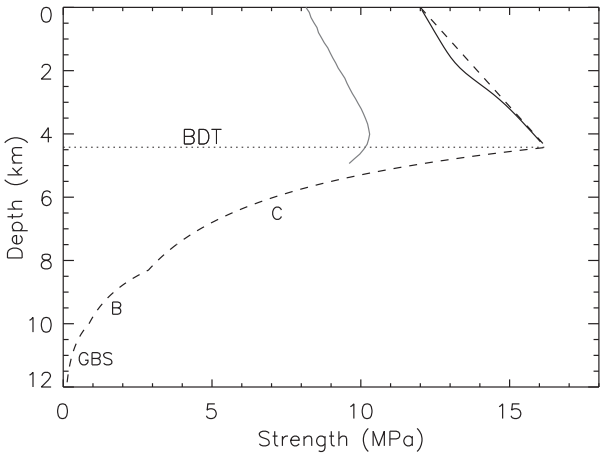

Fig. 2. Initial model strength ($\acute{\sigma}_E$) profile with a thermal gradient of 10 K km^{-1}, a strain rate of 10^{-13} s^{-1}, and a grain size of 1 mm (black line). The theoretical strength profile (in which the frictional portion of the profile is set by Eq. (3) and the viscous portion by Eq. (2)), is also shown (dashed line). The actual frictional strength deviates slightly from the theoretical due to unrelaxed Poisson stresses in the upper lithosphere. The viscous portion of the profile is labeled with the flow mechanism that dominates each segment (dislocation creep C, dislocation creep B, and GBS). The horizontal dashed line at 4.6 km indicates the position of the brittle–ductile transition (BDT). Also shown is the yield strength of the lithosphere after 20% extension for a simulation without strain weakening (gray line), which is reduced from the initial profile due to large tensile stresses in the lithosphere. Note that our strength profiles are related to, but somewhat different from, the usual presentation of differential stress.

4. Results

Fig. 4 shows the development of the groove-like deformation and the distribution of plastic strain with increasing extensional strain for our nominal model ($dT/dz = 10$ K km^{-1}, $\dot{\varepsilon} = 10^{-13}$ s^{-1}) with strain weakening parameters ϵ = 3.0, and a = 0.8. At relatively small strains (3–6%), lithospheric necking similar to that observed in Bland and Showman (2007) appears to control the deformation. Minimal strain localization has occurred. By 12% strain, plastic deformation has clearly been concentrated in multiple narrow zones within each lithospheric pinch; however, the surface deformation still appears quite regular. Only when strains become very large (>18%), do the effects of localization become obvious, resulting in periodic but somewhat irregular surface deformation with strain primarily localized in two regions of the lithosphere. Clearly, with a moderate weakening parameter (ϵ = 3.0) the surface deformation in this simulation is controlled by lithospheric necking, which is enhanced by strain localization. In this case the growth of the necking instability controls the wavelength of the deformation, rather than the growth of a localization instability (cf. Montési

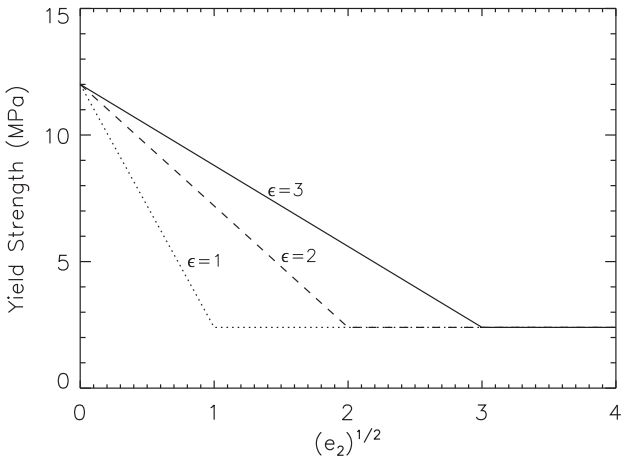

Fig. 3. Heuristic model of strain weakening implemented in the Tekton finite-element model. Models are shown with three different values of ϵ: ϵ = 1.0 (dotted line), ϵ = 2.0 (dashed line), and ϵ = 3.0 (solid line). For each model a = 0.8. See Eq. (7).

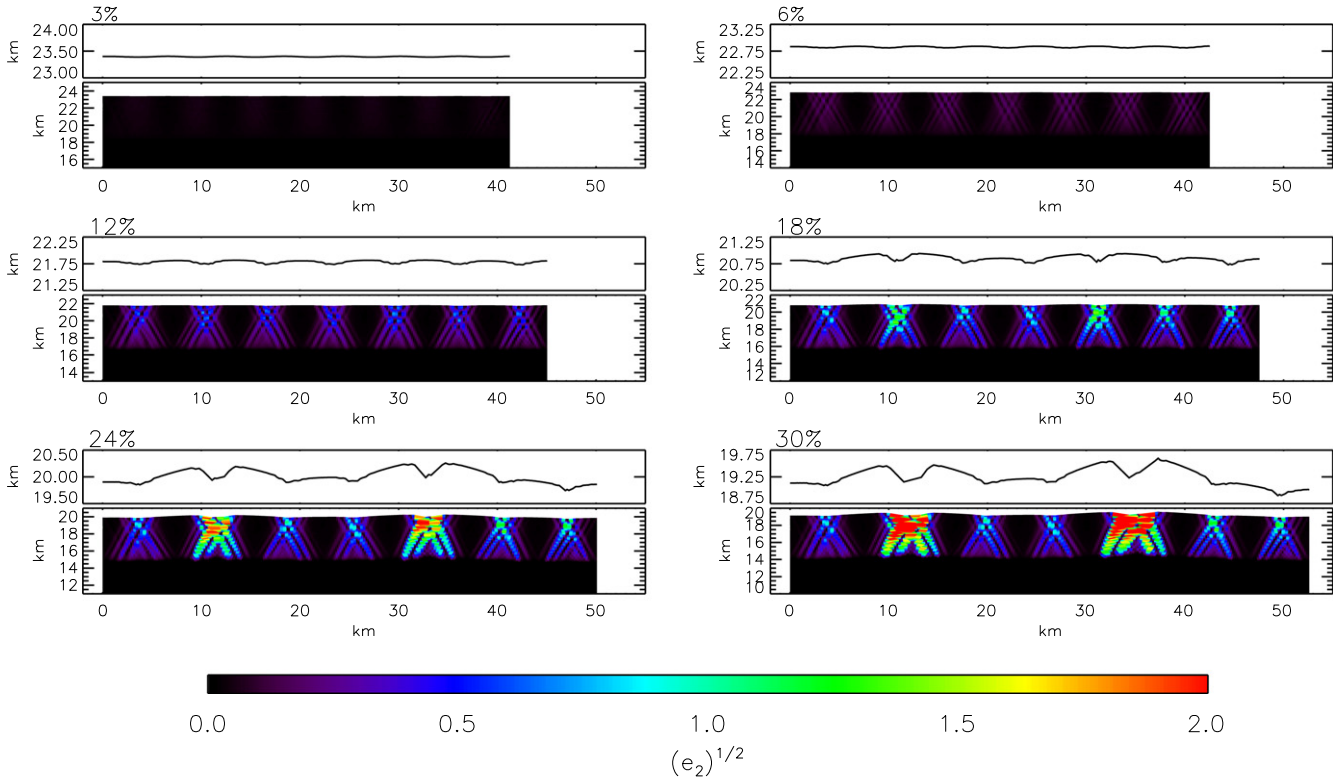

Fig. 4. Square root of the second invariant of the plastic strain and the trace of the surface deformation at 3%, 6%, 12%, 18%, 24% and 30% extensional strain for the nominal model (10 K km^{-1}, 10^{-13} s^{-1}) with strain weakening parameters of $\epsilon = 3.0$, and $a = 0.8$. Strain values in each color map range from 0 (black) to 2.0 (red). The initial perturbation wavelength was 5.7 km (10-m amplitude). Only the top ~10 km of the lithosphere is shown in each panel. The simulation domain is shown without vertical exaggeration and the surface trace is shown with 5× vertical exaggeration. (For interpretation of the references to color in this figure legend, the reader is referred to the web version of this article.)

and Zuber, 2003). As the weakening parameter is decreased and weakening occurs more rapidly with strain, the growth of the localization instability becomes more important (see Section 4.2).

The inclusion of strain weakening greatly increases the amplitude of the deformation that results from extension. Fig. 5 shows the results of two simulation after 20% extension: one that does not include strain weakening (consistent with Bland and Showman (2007)) and one that includes strain weakening ($\epsilon = 3.0$, $a = 0.8$, as shown in Fig. 4). In the simulation without strain weakening (left panels) the surface deformation is extremely regular with an amplitude of ~40 m (after 30% strain, amplitudes reach ~70 m, consistent with the results of Bland and Showman (2007)), and a final wavelength of 6.8 km: the wavelength of the initial perturbation extended by 20%. Plastic strain in this simulation concentrates in regions roughly 4 km wide within the thinned portions of the lithosphere. The maximum plastic strain is 0.37. In contrast, the surface deformation produced when strain weakening is included (right panels) remains periodic but is less regular than that in the simulation without weakening. Average groove amplitudes after 20% strain are ~150 m with maximum amplitudes near

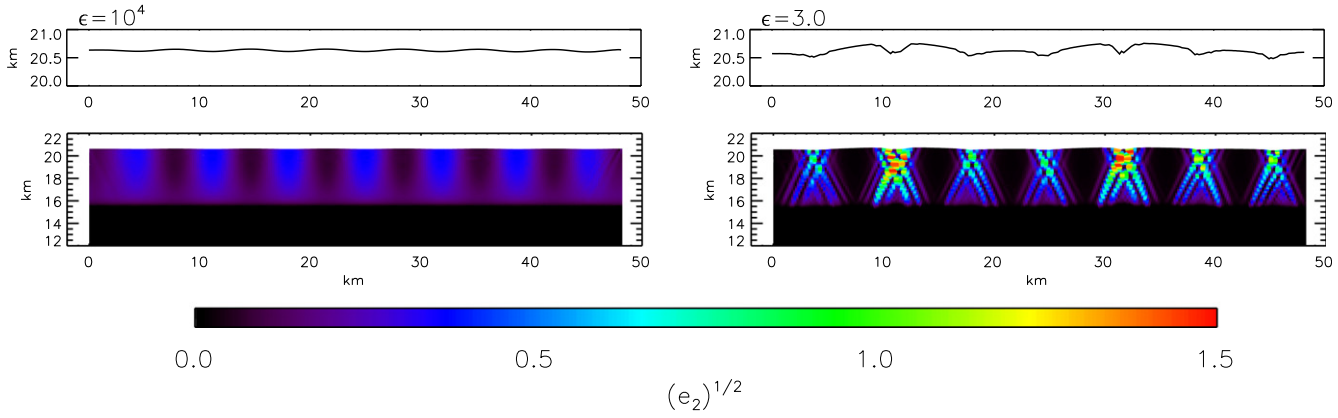

Fig. 5. Comparison of the square root of the second invariant of the plastic strain in each element after 20% extension for a simulation with no strain weakening (*Left*, $\epsilon = 10^4$, $a = 0.8$) and for a simulation with strain weakening (*Right*, $\epsilon = 3.0$, $a = 0.8$), for the nominal model (see parameters in Fig. 4). Strain values in each color map range from zero (black) to 1.5 (red). Only the top ~10 km of each simulation domain is shown. Each model domain is shown without vertical exaggeration. The trace of the surface deformation (with 5× vertical exaggeration) is plotted above each color map. (For interpretation of the references to color in this figure legend, the reader is referred to the web version of this article.)

230 m (average and maximum amplitudes increase to ~250 m and ~500 m, respectively, after 30% strain). Plastic strain again occurs within narrow zones in the necked regions of the ice lithosphere. Within each necked region, however, the plastic strain occurs in multiple, fault-like, linear segments two to four elements in width (333 m to ~2 km). In the near surface, narrow zones of large plastic deformation dip inward at an angle of ~60° until paired, antithetically-dipping zones intersect at a depth of 1–2 km. The dips of the fault-like zones are consistent with dips observed in normal faults (Davis and Reynolds, 1996). The zones continue beyond the intersection point, now dipping away from each other, until approaching the brittle–ductile transition near a depth of ~5 km. The maximum plastic strain in this simulation was 1.6.

We emphasize that these linear zones of high plastic deformation are not true faults, which are not included in the simulation. Rather, they are more analogous to broad zones of distributed faulting (shear zones). We note that the actual width of the fault zones decreases as mesh resolution increases. That is, fault zones are consistently 2–4 elements wide independent of the size of the element (as above). Unfortunately, computation time does not encourage the use of even smaller elements. We believe, however, that it is the mere presence of the fault-like zone of localized plastic deformation and not its width that leads to large-amplitude, complex deformation. Thus, we do not expect an increase in mesh resolution to change our general conclusions in this regard (i.e., offsets should be similar, cf. Lavier et al., 2000).

The inclusion of strain weakening also strongly influences the local stress field and thus the yield strength within the lithosphere. Fig. 6 compares the in-plane shear stress ($\left[\left(\frac{\sigma_{xx}-\sigma_{yy}}{2}\right)^2+\sigma_{xy}^2\right]^{1/2}$, where σ_{xx}, σ_{yy}, and σ_{xy} are the in-plane components of the stress tensor) in each element after 20% extension for the two simulations shown in Fig. 5. In the simulation without weakening, shear stress is broadly distributed, with modest reduction in the necked regions. Maximum stresses occur at a depth of ~5 km, near the brittle–ductile transition. In the near surface, minimum shear stresses occur within the undeformed lithospheric swells. The inclusion of strain weakening strongly enhances the localization of shear stress. Maximum shear now occurs in association with each necked region as much less strain is partitioned into the swells; like the plastic strain, stress is highly localized within deforming necks, occurring in elements immediately adjacent to highly-strained elements. Within the zones of plastic deformation shear stresses are low, especially within the two dominant necks, in part due to the low yield strength associated with these regions (see below), which prevent large stresses. Extremely low shear stress also occurs within the undeformed lithospheric swells near the surface of the domain.

Fig. 7 shows the brittle (or plastic) yield strength of each element after 20% extension for the two simulations described above. In both simulations the yield strength generally increases with increasing depth (i.e., as the mean stress, which is negative

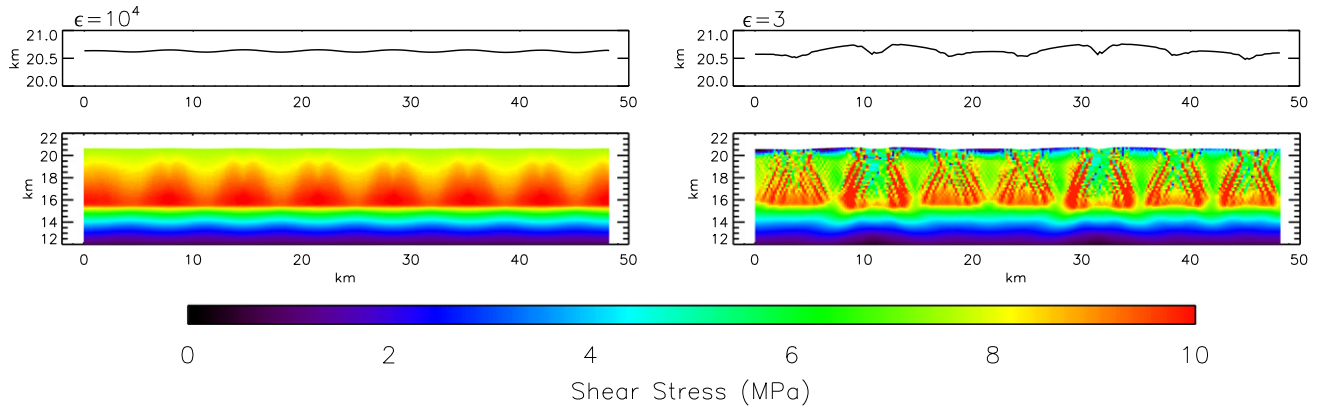

Fig. 6. As in Fig. 5 but for the in-plane shear stress $\left(\left[\left(\frac{\sigma_{xx}-\sigma_{yy}}{2}\right)^2+\sigma_{xy}^2\right]^{\frac{1}{2}}\right)$ in each element. Values of shear stress range from zero (black) to 10 MPa (red). Plots of effective shear stress $(\sqrt{J_2})$ are similar in pattern. (For interpretation of the references to color in this figure legend, the reader is referred to the web version of this article.)

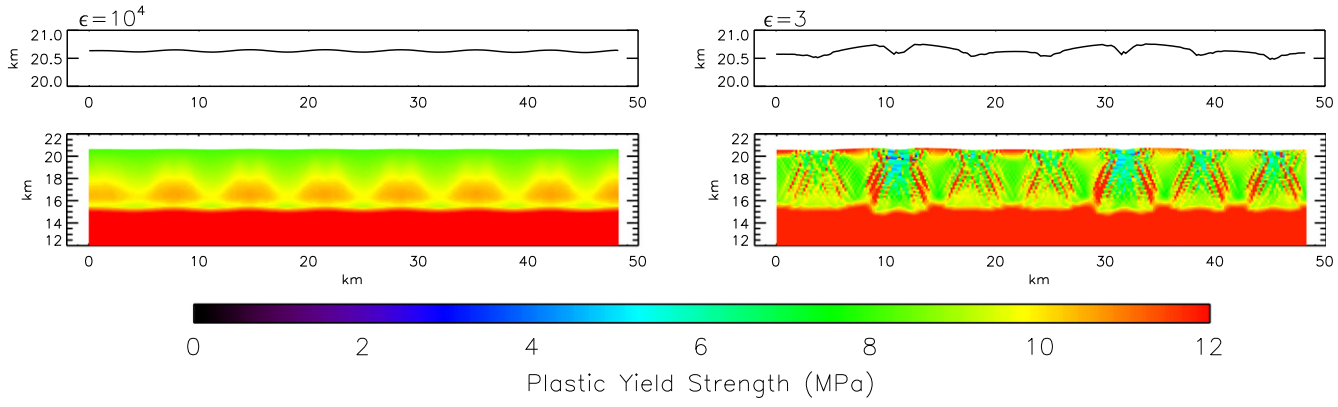

Fig. 7. As in Fig. 5 but for the plastic yield strength (see Eqs. (3) and (7)) in each element. Yield strength values range from 0 (black) to 12 MPa (red). Below the lithosphere, where viscous creep dominates, the plastic yield strength retains its high initial value. (For interpretation of the references to color in this figure legend, the reader is referred to the web version of this article.)

in compression, increases: see Eq. (3)). In the simulation without weakening (left panel), the yield strength is modestly lower than average within the necked regions of the lithosphere (minimum of ~8.0 MPa) because large tensile (positive) stresses are concentrated there. Note that even without weakening, the yield strength is less than that predicted by the initial strength profile (Fig. 2), because of the strong tensile (positive) stresses in the ice lithosphere (see Eq. (3)). When weakening is included (right panel) the pattern of yield strength is more complex. Like the case without weakening, yield strengths are a minimum within the necked, highly deformed portions of the lithosphere; because of the weakening, however, yield strengths in these zones reach values below 2 MPa (after 30% strain, yield strengths drop as low as 800 kPa), nearly an order of magnitude lower than the material's imposed strength at zero pressure (here, effectively 12 MPa). Immediately exterior to the high-deformation zones, and to a lesser degree within the near surface, yield strengths remain high. The higher yield strength in the undamaged portions of the lithosphere inhibits plastic deformation and prevents the narrow zones of plastic deformation from migrating laterally. This effect, coupled with the low yield strength and subsequent large plastic strain within the highly-deformed zones, allows the production of large-amplitude deformation in these simulations.

4.1. Dependence on the thermal gradient

Analytical and numerical models of extensional necking have repeatedly shown that extension produces surface deformation with a wavelength typically 3–4 times the lithospheric thickness, though wavelengths can vary between ~1 and >10 times the lithospheric thickness depending on the strength profile and rheology (e.g., Fletcher and Hallet, 1983; Herrick and Stevenson, 1990; Dombard and McKinnon, 2001; Pollard and Fletcher, 2005, chapter 11; Bland and Showman, 2007; Schmalholz et al., 2008). The thickness of an ice lithosphere is primarily controlled by the lithospheric thermal gradient, which together with the strength envelope sets the depth of the brittle–ductile transition (see Fig. 2). High thermal gradients correspond to thin lithospheres and low thermal gradients correspond to thick lithospheres. Additionally, the growth rate of the necking instability, and the final amplitude of the deformation is also a strong function of the thermal gradient. Analytical models suggest high thermal gradients produce the highest instability growth rates (Herrick and Stevenson, 1990; Dombard and McKinnon, 2001), and at small strain numerical models agree (Zuber and Parmentier, 1996; Bland and Showman, 2007). Bland and Showman (2007) demonstrated, however, that in the limit of large strains ($\geqslant$10%), moderate thermal gradients can actually produce larger amplitude deformation than high thermal gradients because the initial period of rapid growth that occurs at high thermal gradients may not be sustained at finite strain. That is, for similar initial amplitudes, final amplitudes may saturate at lower values in thinner lithospheres. Thus moderate thermal gradients appear optimal for producing large-amplitude grooves.

Our simulations of extensional necking that include strain weakening support the conclusions of Bland and Showman (2007). Fig. 8 shows the surface deformation and second invariant of the plastic strain after 20% extension for four simulations with thermal gradients ranging from 5 to 30 K km^{-1}. Each simulation assumed a moderate $\epsilon = 4.0$ and $a = 0.8$. Maximum deformation amplitudes were achieved in the simulation with a thermal gradient of 10 K km^{-1}. Average deformation amplitudes at higher thermal gradients appear to be limited by the finite thickness of the plastic (i.e., brittle) lithosphere. Not only the final groove amplitude but also the morphology of the deformation appears to vary with thermal gradient. High thermal gradients produce narrow, v-shaped, concave structures while moderate to low thermal gradients produce broad, flat floored, u-shaped convex structures. These morphologies are consistent with the large variety of grooved terrain morphologies observed on Ganymede, which range from large-amplitude ridges-and-troughs, to horst-and-graben, to low-lying areas with regular, subdued troughs in an otherwise flat surface (e.g., Fig. 1 and Patterson et al., 2010).

4.2. Dependence on the rate of strain weakening

The morphology of the surface deformation created by extension depends on the "rate" at which weakening occurs with increasing strain (i.e., how rapidly the yield strength decreases with increasing strain). First, it is useful to examine what we mean by fast and slow changes in yield strength with strain. In an earlier study, Lavier et al. (2000) modeled saturation strains between 0.01 and 4, and similarly to our work retained a fixed residual cohesion, although they did not reduce their internal friction with strain. Saturation strains between ~1 and 4 were considered "moderate," a qualifier we retain. Lavier et al. (2000) argued that fast or rapid loss of cohesion with strain (ϵ of order a few percent), while possibly justifiable from experiments, would not lead to single, large-offset faults and formation of metamorphic core complexes on Earth (which they were studying). Similarly, Wijns et al. (2005) and Gessner et al. (2007) adopted a moderate but somewhat more rapid $\epsilon = 0.5$, with both cohesion and internal friction being proportionally reduced. In contrast, Buck et al. (2003) and Delescluse et al. (2008) used a saturation strain ("equivalent to a critical fault slip") of only 1% and 0.5%, respectively, but the former was strictly an exploratory study and the latter was specifically interested in reactivation of preexisting normal faults at mid-ocean ridges. Here we adopt the perspective of Lavier et al. (2000) that weak natural faults likely form only after considerable damage accumulates over fault length and width. For Ganymede and other icy satellites, however, it is ultimately observations that will best constrain such model parameters as ϵ, a, and whether total strength or cohesion alone should decrease with strain.

Fig. 9 shows the final surface deformation and the plastic strain in the top kilometer of the lithosphere produced by 20% extension for a series of simulations with ϵ varying from 1.0 (rapid weakening with strain) to 6.0 (slow weakening with strain), all for $a = 0.8$. For comparison, a simulation with $\epsilon = 10^4$ (effectively no weakening) is also shown. The thermal gradient in each simulation was 10 K km^{-1}. A slowly decreasing yield strength with strain leads to distributed localization and lower amplitude deformation. An ϵ of 6.0 yields average amplitudes of 85 m and strongly periodic deformation. In contrast, a more rapid decrease in yield strength leads to strain and large-amplitude deformation localizing in only a few locations. An ϵ value of 3.0 results in deformation with maximum amplitudes near 230 m. Much of the deformation is lower in amplitude (~150 m), however, and while still periodic, the topography appears less regular. If weakening occurs rapidly with strain, essentially all of the deformation occurs in a single location. An ϵ of 1.0 produces a single region of extensive deformation consisting of an up-warped region with a central graben-like structure. While some periodic structures exist, they are subdued relative to the much larger graben-like feature. The question of what value of ϵ is appropriate for an ice lithosphere is addressed in the discussion (Section 5).

The dependence of the deformation style on the weakening rate can be intuitively understood by considering how strain localization initiates and depends on the magnitude of the total strain. When weakening is rapid with strain, the first region in which yielding occurs quickly becomes substantially weaker than the rest of the lithosphere. Strain is subsequently accommodated primarily within that region, producing deformation dominated by a single large trough at a relatively small value of total strain. In the

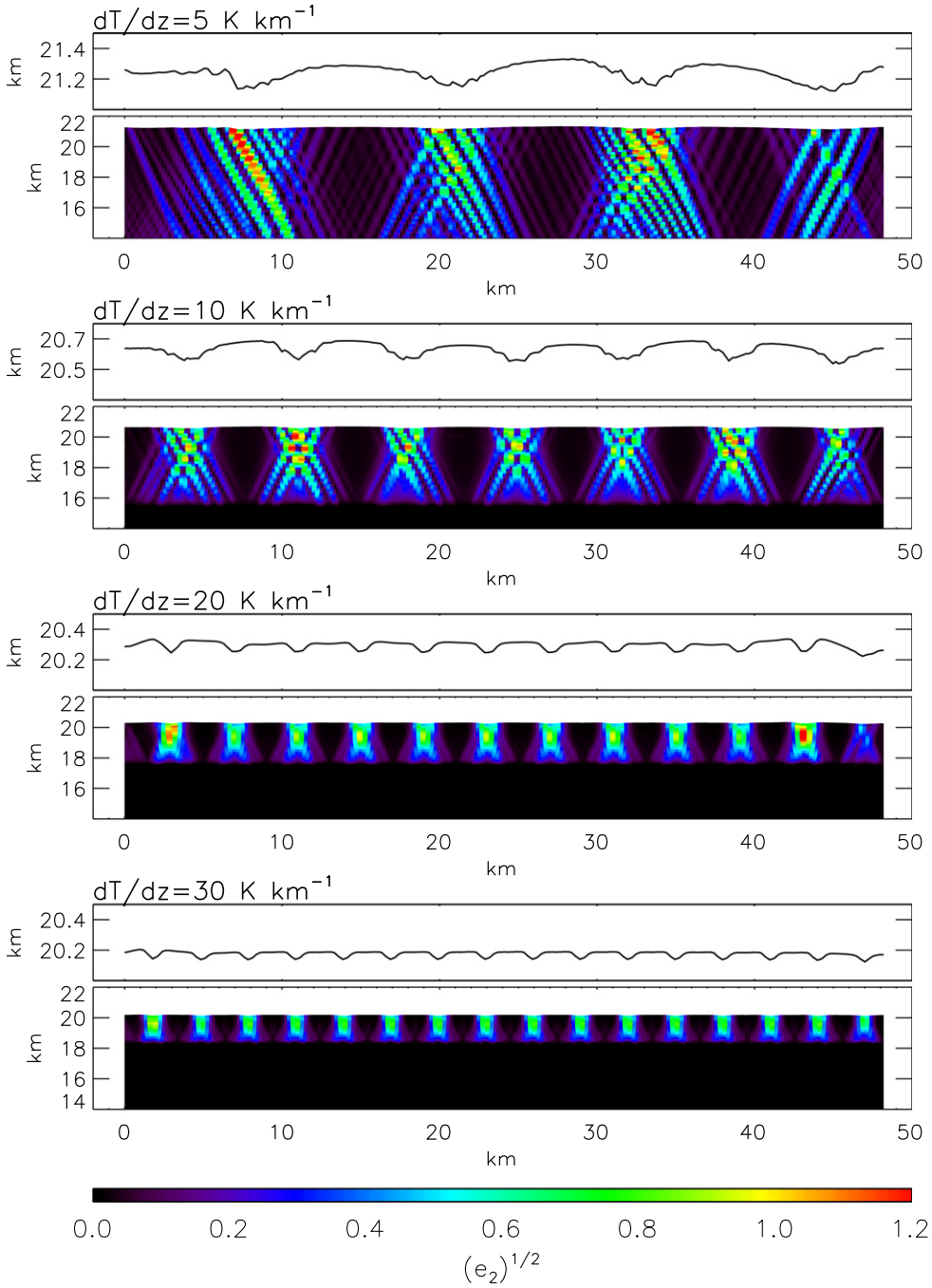

Fig. 8. Surface deformation and second invariant of the plastic strain in the upper ~7 km of the lithosphere after 20% extension for four different thermal gradients (5, 10, 20, and 30 K km^{-1}). Each simulation used weakening parameters of $\epsilon = 4.0$ and $a = 0.8$, and was initialized with sinusoidal topography (amplitude 10 m) with a wavelength appropriate for each thermal gradient: 10.0 km, 5.7 km, 3.3 km, and 2.5 km, respectively (as determined by Bland and Showman (2007)). Each model domain is shown without vertical exaggeration. The trace of the surface deformation (with 10× vertical exaggeration) is plotted above each color map. (For interpretation of the references to color in this figure legend, the reader is referred to the web version of this article.)

simulation with $\epsilon = 1$, the surface deformation is still periodic after 5% strain. However, by 10% strain all of the plastic deformation has been localized into a single region. In this case the growth of the localization instability controls the wavelength of the deformation rather than the growth of a necking instability (cf. Montési and Zuber, 2003). When weakening occurs slowly with strain, the first regions to undergo plastic deformation become only marginally weaker than the surrounding lithosphere. Thus the magnitude of total strain that can be accommodated throughout the entire lithosphere remains large. Eventually several regions (generally the pinched regions of the lithosphere where stresses are highest) become substantially weaker than the surrounding material and strain localizes within these zones, producing distributed but large-amplitude deformation. When $\epsilon = 3$ the surface deformation remains strongly periodic until 12% strain. Only after 18% strain has deformation been localized into just a few regions (Fig. 4). The wavelength of the deformation is controlled by the necking instability as described above (Section 4). In contrast, when $\epsilon = 6$ the deformation is still strongly periodic after 20% (or even 30%) strain. In this case, localization plays a minimal role. Without the

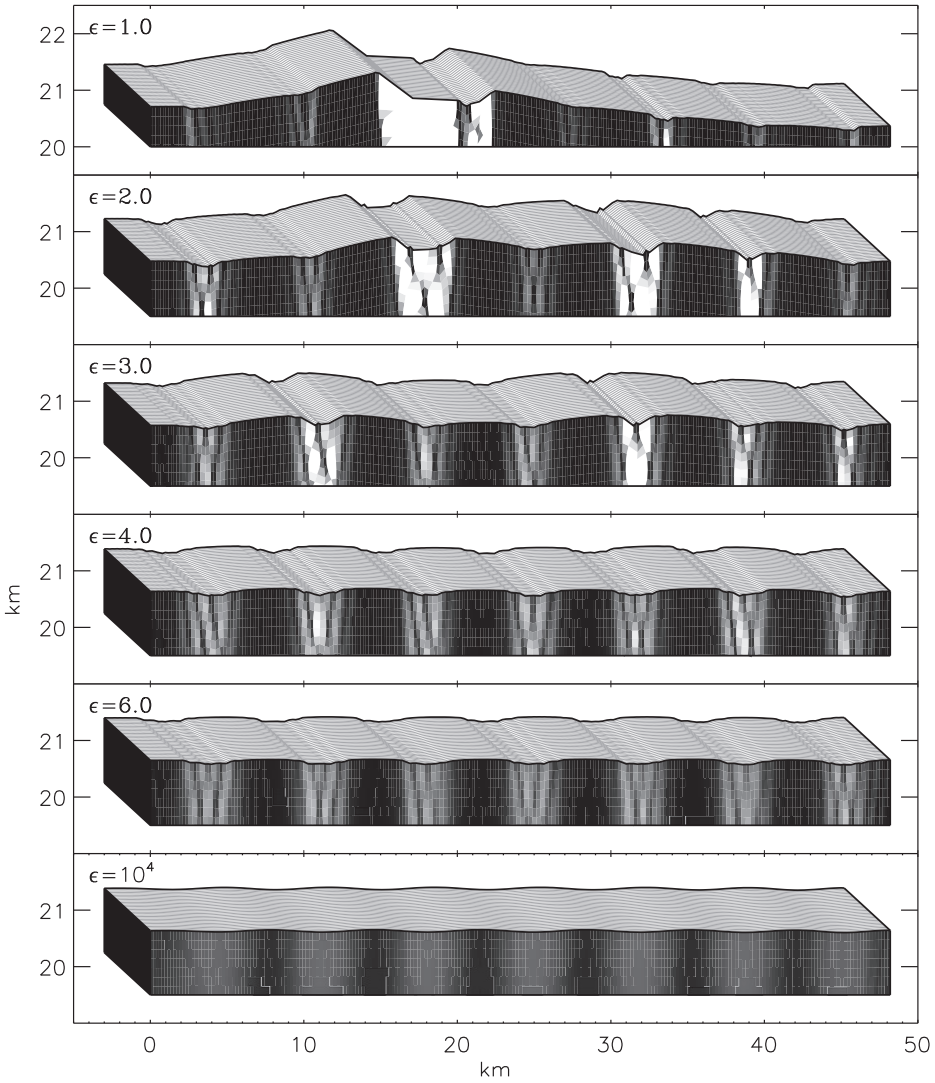

Fig. 9. Surface deformation and the strain in the top kilometer of the lithosphere after 20% extension for six simulations with identical physical parameters (e.g., thermal gradient and strain rate) but different rates of weakening with strain (i.e., different values of ϵ in Eq. (7)). Values of ϵ range from 1.0 (rapid weakening with strain) to 6.0 (slow weakening with strain). For comparison, the surface deformation from a simulation with no weakening $\epsilon = 10^4$ is also shown. The trace of the surface deformation generated by our two-dimensional (x–y) model has been extrapolated into the third dimension to provide a sense of how the corresponding surface might appear. Within the lithosphere, dark shades corresponds to near zero plastic strain and bright shades correspond to high plastic strain (the color scale saturates at $e_2^{\frac{1}{2}} = 1.2$). Initial perturbation wavelength was 5.7 km in all cases. Vertical exaggeration is 4×.

inclusion of weakening, strain is only localized by the increased stress concentrations within the lithospheric pinches, and deformation amplitudes remain low. These results are qualitatively consistent with those of Lavier et al. (1999, 2000), who found a similar dependence on weakening rate and the formation of single large-offset faults versus multiple small-offset faults (although in their case the cohesion but not the internal friction decreased with strain).

That the surface morphology produced by extension depends on both the rate at which yield strength decreases with increasing plastic strain and the total plastic strain has important implications for our understanding of groove terrain formation. Previous modeling (e.g. Fink and Fletcher, 1981; Dombard and McKinnon, 2001; Bland and Showman, 2007) suggested that the wavelength of Ganymede's grooved terrain is directly related to the thermal gradient in Ganymede's lithosphere. In contrast we find that, while the lithospheric thermal gradient sets the initial dominant wavelength, rapid to moderate weakening of the ice can lead to strong localization that may ultimately mask the thermal-gradient-induced periodicity. Rapid weakening can result in non-periodic or even singular deformation; even moderate rates of weakening can result in deformation that is only quasi-periodic. One must therefore use caution when attempting to determine ancient thermal gradients using topographic wavelengths alone (i.e., amplitude and phase may be important diagnostics as well). Of course, the more regular and periodic the topography of a given grooved terrain set, the more direct the relationship between the dominant groove spacing and the lithospheric thermal gradient at the time of its formation.

Groove morphology results from the interplay between thermal-gradient-induced topographic wavelengths and the formation of weak zones within the lithosphere and near surface. The resulting surface deformation is significantly more complex than that produced in models that do not include weakening (Bland and Showman, 2007). Such complex surface deformation is, however, more consistent with observations of Ganymede's actual grooves.

4.3. Dependence on the initial perturbation

For simplicity, the simulations described above use an initial topographic perturbation consisting of a single sinusoid with a

wavelength equal to that expected for a thermal gradient of 10 K km^{-1} (based on the modeling of Bland and Showman (2007)). However, Ganymede's pre-grooved surface topography would have been complex, containing a spectrum of wavelengths. Previous modeling has shown that unstable extension will successfully establish the expected dominant wavelength even when the initial surface perturbation consists of semi-random topography (Bland and Showman, 2007). When strain weakening is permitted, however, the development of the expected dominant wavelength is not guaranteed because the early formation of weak zones in the preexisting topography may disrupt its establishment.

To determine whether periodic deformation can result from non-periodic initial topography in the presence of strain weakening, we performed a series of simulations that utilized semi-random initial topography. The initial topographic perturbation consisted of 17 wavelengths ranging from 1.4 to 20 km that were given a random phase shift, added together, and normalized to have a maximum amplitude of 15 m. Fig. 10 shows the final surface deformation after 20% strain, the distribution of plastic strain at depth, and the Fourier spectrum of the surface deformation for four simulations that included such semi-random initial topography and rates of strain weakening that varied from $\epsilon = 10^4$ (i.e., no weakening) to $\epsilon = 3$. The thermal gradient in each simulation was 10 K km^{-1}. The simulation with no strain weakening resulted in low-amplitude but strongly periodic deformation. The corresponding Fourier spectrum indicates that the surface deformation primarily contains wavelengths near 6.5 km, confirming the results of Bland and Showman (2007). Fig. 10 further indicates that, as the rate of weakening with strain increases, extension consistently produces deformation with a dominant wavelength near 6.5 km. For more rapid weakening with strain, isolated, long-wavelength deformation begins to dominate the topography, though the signature of the 6.5-km-deformation is still observed. The long wavelength features occur at ~25 km (i.e., half the domain length) and correspond to deformation not associated with individual grooves.

The distribution of plastic strain at depth clearly indicates that when weakening occurs at a moderate rate with strain ($\epsilon = 3$), strain will localize in just a few regions (see Fig. 9). Additionally, Fig. 10 indicates that when weakening occurs at a moderate rate the distribution of plastic strain depends, to some extent, on the initial topography. Strain preferentially localizes where the initial topography is deeper or broader than average. Thus, even when the same wavelengths are used to construct the initial topography, changing the phase shift applied to each wavelength results in changes to the final deformation after extension. The dependence on the initial topography is not observed when strain weakening is not included in the simulation (Bland and Showman, 2007). These results suggest that if weakening occurs slowly unstable

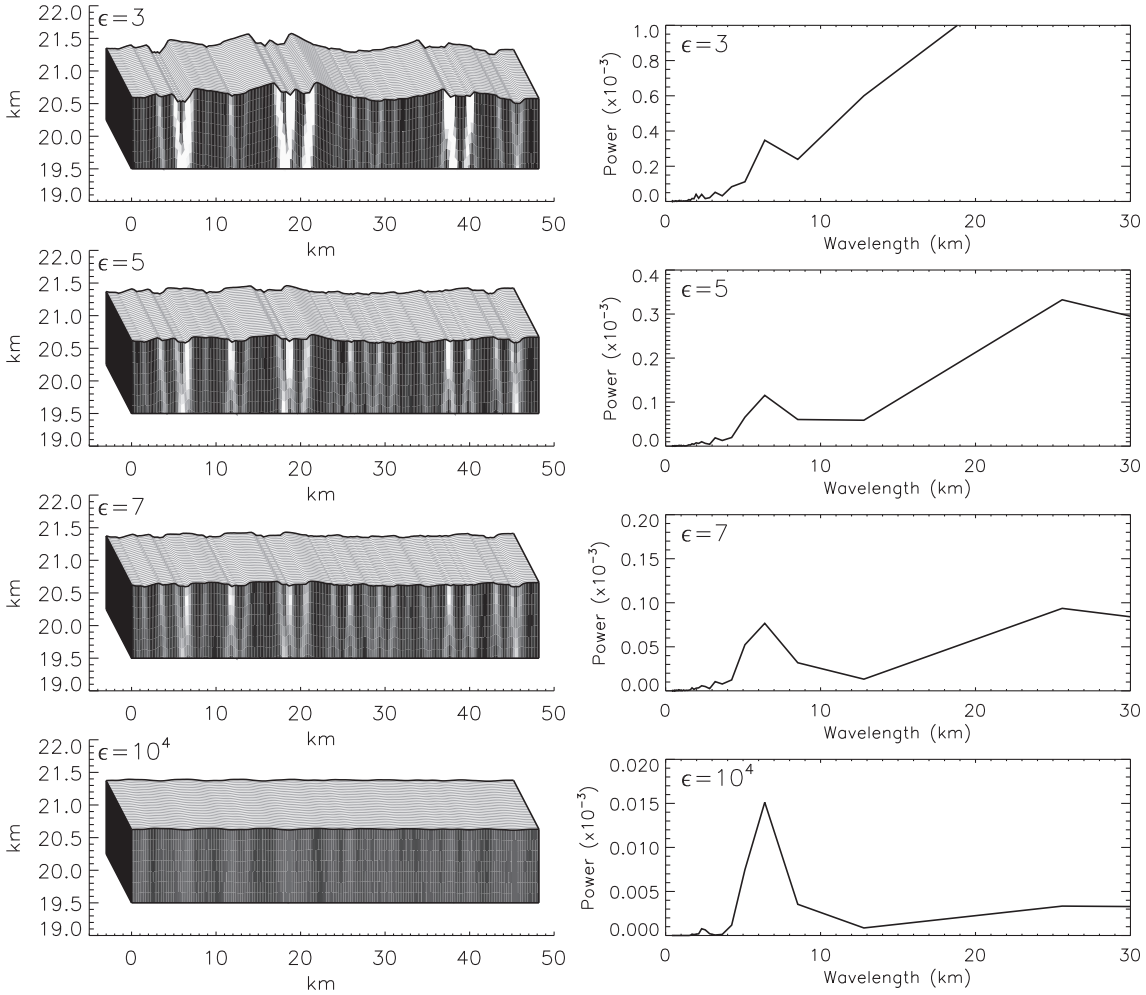

Fig. 10. Deformation after 20% extension for simulations that utilize a semi-random initial surface topography (see text) and varying rates of strain weakening ($\epsilon = 3$, 5, 7, 10^4). The thermal gradient was 10 K km^{-1} in each simulation. The left column shows the surface deformation and the distribution of plastic strain at depth for each simulation (light regions indicate high strain, dark regions indicate low strain). Vertical exaggeration is 9×. The right column shows the Fourier spectrum of the surface deformation in the simulation to its left.

extension can select and preferentially amplify a single dominant wavelength of topography, producing periodic deformation that is independent of the initial topographic perturbation. If, however, weakening occurs moderately or rapidly with strain, the resulting deformation is less periodic and is dominated by strong localization in a few regions, the locations of which are, in part, controlled by the initial topography. Producing groove-like features therefore again depends sensitively on the weakening rate: too slow and the deformation is periodic but may be low-amplitude, too fast and the deformation is large-amplitude but may be non-periodic.

Finally, we note that if even small-amplitude (15 m) initial topography can affect the form of the final surface deformation, it remains unclear how periodic structures form in the presence of large-amplitude, short-wavelength topography (e.g., crater rims or furrows) (see Bland and Showman, 2007). We have not addressed this issue explicitly, but imbricately faulted (i.e., grooved) craters on Ganymede are known (Pappalardo and Collins, 2005), and groove formation by means of extensional instability in Ganymede's dark terrain is theoretically possible (Dombard and McKinnon, 2001). In these cases the initial topography may or may not still be discerned, the amplitude of the extensional instability is arguably less, and the resulting overall morphological pattern not nearly as regular and symmetrical (as in, e.g., Fig. 1). Implicit in our modeling of bright grooved terrain is that groove formation initiates on relatively level terrain, due either to cryovolcanic flooding of lithospheric rifts or formation of dilational bands (see Pappalardo et al. (2004) and Collins et al. (2010), for discussion).

5. Discussion and conclusions

We have produced a numerical model that, for the first time, yields surface deformation that is reasonably consistent with the morphologies of Ganymede's grooved terrain. In contrast to previous modeling (Bland and Showman, 2007), the inclusion of strain weakening (i.e., the decrease in yield strength with increasing plastic strain) results in grooves with peak-to-trough amplitudes of 200–500 m (at least for the parameters explored here). The increase in deformation amplitude can be directly attributed to strain localization due to the loss of material strength within thinned regions of the lithosphere. We find that the morphology of the surface deformation depends not only on the prescribed thermal gradient but also on the rate at which weakening occurs with strain. The local thermal gradient sets the prevailing topographic wavelength of each groove swath; each groove trough, however, is associated with a narrow zone of shear deformation and relatively deep-seated faulting. As extension continues, the amplitude of the deformation (i.e., the magnitude of the local strain) and the strength of the periodicity is controlled by how rapidly the ice weakens with strain. Large graben-like structures might occur where ice is easily weakened, whereas low-amplitude periodic structures might occur where the ice can retain its strength. Thus, extension can result in complex surface deformation. The production of such complex deformation is consistent with high-resolution observations of grooved terrain that indicate different groove morphologies can occur in proximity to one another (Pappalardo et al., 1998, Fig. 1).

The question remains as to why the ice lithosphere would weaken at one rate with strain in some regions but at a different rate in others, producing the range of groove morphologies observed. Our simple, heuristic model of ice weakening is insufficient to fully address this question, but reasonable hypothesis can be advanced. Images of Ganymede's surface indicate that many grooved regions have experienced repeated episodes of deformation (e.g., Collins et al., 1998a). The local strain history of the ice may therefore control weakening rates, with more rapid weakening through fault reactivation occurring in regions with a long history of tectonic deformation. The thermal history of the lithosphere may be equally important, as periods of high heat flow may contribute to annealing and strengthening the ice locally.

Like Bland and Showman (2007), our modeling indicates that high thermal gradients ($\sim$30 K km^{-1} (Dombard and McKinnon, 2001)) may not be required to produce Ganymede's large-amplitude grooves. Instead, moderate thermal gradients ($\sim$10 K km^{-1}) may be sufficient to explain much of the observed deformation. Such thermal gradients imply a heat flow of $\sim$50 mW m^{-2} (assuming a thermal conductivity of ice that varies as $k = (651\ \mathrm{W\ m^{-1}})/T$ (Petrenko and Whitworth, 1999, p. 43), where T is the temperature (see Bland et al., 2007)). While smaller than the heat fluxes suggested by Dombard and McKinnon (2001), a heat flux of $\sim$50 mW m^{-2} is still a factor of two greater than the maximum heat flux that could have been produced by radiogenic heating alone (Bland et al., 2009). Additional energy may have been provided by a period of tidal dissipation (Showman et al., 1997; Bland et al., 2009), cryovolcanic eruptions or intrusions (Herrick and Stevenson, 1990; Dombard and McKinnon, 2001), Europa-like dilational band formation (Head et al., 2002; Prockter and Patterson, 2009), or convective overturn, such as has been proposed for Enceladus (Barr, 2008; O'Neill and Nimmo, 2010). Heat flow may also be lower for the same temperature gradients if the thermal conductivity of ice is reduced from its laboratory value, which seems almost assured for fractured ice.

Understanding the diversity of tectonic features observed on icy satellites remains one of the over-arching challenges in outer Solar System geology and geophysics. The satellites Ganymede, Europa, Enceladus, Tethys, Dione, Rhea, Miranda, Ariel, and Titania all exhibit tectonic features that likely formed in extension (Collins et al., 2010). Yet the morphology of deformation on these satellites covers a broad range, with some features unique to a given body (or nearly so). The modeling described here cannot fully account for the panoply of icy satellite tectonic deformation, but it does provide important clues. We have shown that the deformation of an ice lithosphere depends on more than just the immediate physical conditions of the ice shell (e.g., the thermal gradient, strain rate, strain magnitude). Rather, it can depend sensitively on the detailed mechanical behavior and strain history of the ice lithosphere. Understanding the origin of surface features on icy satellites will therefore require careful consideration of these factors.

In addition, while we have made important gains in understanding groove formation, a number of important problems remain unaddressed. The periodic, quasi-parallel structures observed in the grooved terrain indicate that ductile extensional deformation at depth (i.e., extensional necking) is an essential component of groove formation; the surface morphology observed by spacecraft, however, has primarily resulted from brittle deformation of near surface ice in response to extension and necking. Our model handles such deformation with a continuum approach that does not resolve the details of important physical processes such as the formation of fine-scale, discrete faults (the "faults" illustrated in Figs. 4–10 are best thought of as shear zones). Evaluating how well numerical models reproduce the small-scale details of groove morphology, and addressing whether extension can completely disrupt the preexisting, heavily-cratered surface so that it is unrecognizable (see Head et al., 1997) therefore remains for future work. We also note that while unstable extension occurs naturally in two-dimensional models, it remains unclear how ridges-and-troughs that are continuous for hundreds of kilometers along strike form from random, three-dimensional surface topography (though see Fletcher, 1995).

Several other aspects of our modeling effort deserve comment. First, our numerical model uses a cohesion for ice an order of magnitude higher than the experimental value: 10 MPa as opposed to the nominal 1 MPa as measured by Beeman et al. (1988). Further,

the value of Beeman et al. (1988) is likely still larger than the actual strength of an ice lithosphere that is pre-fractured by impacts, thermoelastic stress, tides, or any number of other processes (in the absence of annealing). A weak lithosphere is also supported by observations: the formation of Europa's cycloidal cracks, for example, may require tensile strength of only ~10 kPa (Hoppa et al., 1999). We chose to use a high cohesion for numerical stability, and to facilitate direct comparisons to Bland and Showman (2007). Use of such a high cohesion introduces several complications, however. A large cohesion value results in a very stiff lithosphere that should permit increased necking during extension in the presence of strain weakening, but the large cohesion also results in very high values of stress at the brittle–ductile transition. Ice deforming ductilely at such high stress will do so by dislocation creep in the C regime (see Fig. 2), a relatively stiff deformation mechanism (Durham and Stern, 2001), rather than the less viscous dislocation B or GBS regime. Dombard and McKinnon (2001) found that it was precisely the inclusion of the less viscous, grain-size-sensitive creep mechanisms that permitted large growth rates during extension. In addition, the influence of ductile C is exacerbated by the low surface temperature (70 K) adopted in the calculation here, given that surface temperature has a direct influence on the temperature at the BDT. Until numerical models implement more realistic cohesion and surface temperature values, a complete understanding of groove formation via unstable extension will not be achieved.

Second, in simulations that include weakening (especially when $\epsilon < 3$) elements within the "shear zones" become highly deformed. This deformation is due both to the strong localization of strain, and dilation (i.e., bulking) due to our plastic failure model (see below). Highly deformed elements can result in large numerical uncertainty, leading to unrealistic results (see Steele (1989), chapter 8, for more discussion). In our simulations, strain generally localizes in 2–4 elements, independent of their size (cf. Lavier et al., 2000). Thus, increasing the mesh resolution (decreasing element size) cannot alleviate the problem (in fact, finer mesh resolution leads to an increase in relative local strain). In simulations that include rapid to moderate weakening with strain, and impose large total strains, highly deformed elements might only be avoided by utilizing a remeshing scheme. Such a task is beyond the work reported here. For this reason, and because of the effects of dilation (see below), the results presented here need to be viewed more as indicative than absolute (especially for lower ϵ). Our fundamental conclusions are sound, however.

Third, our use of plasticity allows us to approximate the yielding of the lithosphere due to distributed brittle faulting. As in Bland and Showman (2007), not all lithospheric elements are in failure at the same time (see their Fig. 3). At any given time most of the lithosphere, while close to yielding, is actually behaving elastically. In this way, the rheological behavior of our model lithosphere more resembles the fiber-bundle or damage rheology model of Turcotte and Glasscoe (2004) and Nanjo et al. (2005) for the upper continental crust. The later estimated the effective power-law exponent n of the upper crust to be ~6, that is, large but not infinitely large. Schmalholz et al. (2008) have shown, in their studies of extending power-law layers, that both the rate and wavelength of maximum selective pinch-and-swell amplification depend on n. In particular, as n declines from values appropriate to perfect plasticity ($n \to \infty$) to values more appropriate to a damaged brittle layer, the rate of amplification (instability factor q in Bland and Showman (2007) and Dombard and McKinnon (2001)) declines considerably. Although we do not estimate the effective n for our extending lithospheres here, this may be another reason why the overall q values in Bland and Showman (2007) are so much lower than those derived from analytical models in Dombard and McKinnon (2001). The lower effective n appropriate to a damage rheology may, however, be more appropriate to an extending lithosphere than one of near perfect plasticity.

Fourth, the implementation of plasticity in the Tekton finite-element code uses the so-called "associated flow rule." In this model, once stresses reach the yield surface (Eq. (3)), a plastic strain-rate normal to that surface acts to keep the stresses there. This seemingly arcane procedure is standard in metallurgical or materials science plasticity (e.g., Owen and Hinton, 1980), but for frictional materials (soils, concrete) leads to dilation or bulking (e.g., Poliakov and Herrmann, 1994). Some dilation upon fracture and/or cataclasis in brittle materials is expected, but it is limited. For geological continuum models undergoing large finite extension, especially in the pinched or necked regions, the amount of strain that can be realistically modeled using the associated flow rule is likewise limited. In our simulations with $\epsilon \leqslant 2$, some elements have dilated well beyond what would be realistic for a geologic material. Again, we emphasize that the results described here capture the important behavior of strain localization in an extending ice lithosphere, but should not be viewed as absolute. Future work will incorporate an incompressible, non-associative plastic flow rule.

Despite these lingering questions, our modeling has produced surface deformation comparable to Ganymede's grooved terrain and yielded new insight into the groove formation process. Furthermore, the importance of strain localization in explaining the formation of Ganymede's grooved terrain highlights the importance of localization in icy satellite tectonics. Strain localization is therefore likely to contribute to the formation of surface features found throughout the satellites of the outer Solar System.

Acknowledgments

We thank Paul Schenk for Fig. 1. Laurent Montési and Geoffrey Collins provided thoughtful reviews. This work was supported by NASA Planetary Geology and Geophysics Grant Number NNX08AM42G and Outer Planets Research Grant Number NNX09AP32G.

References

Barr, A.C., 2008. Mobile lid convection beneath Enceladus' south polar terrain. J. Geophys. Res. 113, 7009. doi:10.1029/2008JE003114.

Barr, A.C., McKinnon, W.B., 2007. Convection in ice I shells and mantles with self-consistent grain size. J. Geophys. Res. 112, E02012. doi:10.1029/2006JE002781.

Beaumont, C., Kamp, P.J.J., Hamilton, J., Fullsack, P., 1996. The continental collision zone, South Island, New Zealand: Comparison of geodynamical models and observations. J. Geophys. Res. 101, 3333–3360. doi:10.1029/95JB02401.

Beeman, M., Durham, W.B., Kirby, S.H., 1988. Friction of ice. J. Geophys. Res. 93, 7625–7633.

Bercovici, D., 1995. A source-sink model of the generation of plate tectonics from non-Newtonian mantle flow. J. Geophys. Res. 100, 2013–2020.

Bercovici, D., 1996. Plate generation in a simple model of lithosphere–mantle flow with dynamic self-lubrication. Earth Planet. Sci. Lett. 144, 41–51. doi:10.1016/0012-821X(96)00140-9.

Bland, M.T., Beyer, R.A., Showman, A.P., 2007. Unstable extension of Enceladus' lithosphere. Icarus 192, 92–105. doi:10.1016/j.icarus.2007.06.011.

Bland, M.T., Showman, A.P., 2007. The formation of Ganymede's grooved terrain: Numerical modeling of extensional necking instabilities. Icarus 189, 439–456. doi:10.1016/j.icarus.2007.01.012.

Bland, M.T., Showman, A.P., Tobie, G., 2009. The orbital–thermal evolution and global expansion of Ganymede. Icarus 200, 207–221. doi:10.1016/j.icarus.2008.11.016.

Braun, J., Chéry, J., Poliakov, A., Mainprice, D., Vauchez, A., Tomassi, A., Daignières, M., 1999. A simple parameterization of strain localization in the ductile regime due to grain size reduction: A case study for olivine. J. Geophys. Res. 104, 25167–25181.

Brun, J.P., Cobbold, P.R., 1980. Strain heating and thermal softening in continental shear zones: A review. J. Struct. Geol. 2, 149–158.

Buck, W.R., Lavier, L.L., Babeyko, A., 2003. A numerical model of lithospheric extension producing fault-bounded basins and ranges. Int. Geol. Rev. 18, 712–723.

Buck, W.R., Poliakov, A.N.B., 1998. Abyssal hills formed by stretching oceanic lithosphere. Nature 392, 272–275.

Collins, G.C., 2008. Driving mechanisms for grooved terrain formation on Ganymede: Comparison of theory to global groove database. Lunar Planet. Sci. 39. Abstract 2254.

Collins, G.C., Head, J.W., Pappalardo, R.T., 1998a. Formation of Ganymede grooved terrain by sequential extensional episodes: Implications of Galileo observations for regional stratigraphy. Icarus 135, 345–359.

Collins, G.C., Head, J.W., Pappalardo, R.T., 1998b. The role of extensional instability in creating Ganymede grooved terrain: Insights from Galileo high-resolution stereo imaging. Geophys. Res. Lett. 25, 233–236. doi:10.1029/97GL03772.

Collins, G.C., McKinnon, W.B., Moore, J.M., Nimmo, F., Pappalardo, R.T., Prockter, L.M., Schenk, P.M., 2010. Tectonics of the outer planet satellites. In: Watters, T.R., Schultz, R.A. (Eds.), Planetary Tectonics. Cambridge University Press, pp. 264–350.

Davis, G.H., Reynolds, S.J., 1996. Structural Geology of Rocks and Regions. John Wiley & Sons, Inc., New York.

Delescluse, M., Montési, L.G.J., Chamot-Rooke, N., 2008. Fault reactivation and selective abandonment in the oceanic lithosphere. Geophys. Res. Lett. 35. doi:10.1029/2008GL035066.

Dombard, A.J., McKinnon, W.B., 1996. Formation of grooved terrain on Ganymede: Extensional instability mediated by cold, diffusional creep. Lunar Planet. Sci. XXVII, 317–318.

Dombard, A.J., McKinnon, W.B., 2001. Formation of grooved terrain on Ganymede: Extensional instability mediated by cold, superplastic creep. Icarus 154, 321–336. doi:10.1006/icar.2001.6728.

Durham, W.B., Stern, L.A., 2001. Rheological properties of water ice: Applications to satellites of the outer planets. Annu. Rev. Earth Planet. Sci. 29, 295–330. doi:10.1146/annurev.earth.29.1.295.

Fink, J.H., Fletcher, R.C., 1981. Variations in thickness of Ganymede's lithosphere determined by spacings of lineations. Lunar Planet. Sci. XII, 277–278.

Fleitout, L., Froidevaux, C., 1980. Thermal and mechanical evolution of shear zones. J. Struct. Geol. 2, 159–164.

Fletcher, R., 1995. Three-dimensional folding and necking of a power-law layer: Are folds cylindrical, and, if so, do we understand why? Tectonophysics 247, 65–83. doi:10.1016/0040-1951(95)00021-E.

Fletcher, R.C., Hallet, B., 1983. Unstable extension of the lithosphere: A mechanical model for basin-and-range structure. J. Geophys. Res. 88, 7457–7466.

Frederiksen, S., Braun, J., 2001. Numerical modeling of strain localisation during extension of the continental lithosphere. Earth Planet. Sci. Lett. 188, 241–251.

Gammon, P.H., Klefte, H., Clouter, M.J., 1983. Elastic constants of ice samples by Brillouin spectroscopy. J. Phys. Chem. 87, 4025–4029.

Gerbault, M., 2000. At what stress level is the central Indian Ocean lithosphere buckling? Earth Planet. Sci. Lett. 178, 165–181.

Gessner, K., Wijns, C., Moresi, L., 2007. Significance of strain localization in the lower crust for structural evolution and thermal history of metamorphic core complexes. Tectonics 26, TC2012. doi:10.1029/2004TC001768.

Giese, B., Oberst, J., Roatsch, T., Neukum, G., Head, J.W., Pappalardo, R.T., 1998. The local topography of Uruk Sulcus and Galileo Regio obtained from stereo images. Icarus 135, 303–316. doi:10.1006/icar.1998.5967.

Goldsby, D.L., Kohlstedt, D.L., 1997. Flow of ice I by dislocation, grain boundary sliding, and diffusion processes. Lunar Planet. Sci. XXVIII, 429–430.

Goldsby, D.L., Kohlstedt, D.L., 2001. Superplastic deformation of ice: Experimental observations. J. Geophys. Res. 106, 11017–11030. doi:10.1029/2000JB900336.

Golombek, M.P., Banerdt, W.B., 1986. Early thermal profiles and lithospheric strength of Ganymede from extensional tectonic features. Icarus 68, 252–265. doi:10.1016/0019-1035(86)90022-9.

Grimm, R.E., Squyres, S.W., 1985. Spectral analysis of groove spacing on Ganymede. J. Geophys. Res. 90, 2013–2021.

Head, J., and 10 colleagues, 2002. Evidence for Europa-like tectonic resurfacing styles on Ganymede. Geophys. Res. Lett. 29 (24), 4-1. doi:10.1029/2002GL015961.

Head, J.W., Pappalardo, R.T., Collins, G., Greeley, R., 1997. Tectonic resurfacing on Ganymede and its role in the formation of grooved terrain. Lunar Planet. Sci. XXVIII, 535–536.

Herrick, D.L., Stevenson, D.J., 1990. Extensional and compressional instabilities in icy satellite lithospheres. Icarus 85, 191–204. doi:10.1016/0019-1035(90)90110-U.

Hoppa, G.V., Tufts, B.R., Greenberg, R., Geissler, P.E., 1999. Formation of cycloidal features on Europa. Science 285, 1899–1902.

Huismans, R.S., Beaumont, C., 2002. Asymmetric lithospheric extension: The role of frictional plastic strain softening inferred from numerical experiments. Geology 30, 211–214.

Huismans, R.S., Beaumont, C., 2003. Symmetric and asymmetric lithospheric extension: Relative effects of frictional-plastic and viscous strain softening. J. Geophys. Res. 108. doi:10.1029/2002JB002026.

Huismans, R.S., Buiter, S.J.H., Beaumont, C., 2005. Effect of plastic–viscous layering and strain softening on mode selection during lithospheric extension. J. Geophys. Res. 110. doi:10.1029/2004JB003114.

Jin, D., Karato, S., Obata, M., 1998. Mechanisms of shear localization in the continental lithosphere: Inference from the deformation microstructures of peridotites from the Ivrea zone, northwestern Italy. J. Struct. Geol. 20, 195–209.

Kaus, B.J.P., Podladchikov, Y.Y., 2006. Initiation of localized shear zones in viscoelastoplastic rocks. J. Geophys. Res. 111. doi:10.1029/2005JB003652.

Lachenbruch, A.H., Sass, J.H., 1980. Heat flow and energetic of the San Andreas fault zone. J. Geophys. Res. 85, 6185–6223. doi:10.1029/JB085iB11p06185.

Lavier, L.L., Buck, W.R., Poliakov, A.N.B., 1999. Self-consistent rolling-hinge model for the evolution of large-offset low-angle normal faults. Geology 27, 1127–1130.

Lavier, L.L., Buck, W.R., Poliakov, A.N.B., 2000. Factors controlling normal fault offset in an ideal brittle layer. J. Geophys. Res. 105, 23431–23442. doi:10.1029/2000JB900108.

Lemaître, J., 1992. A Course on Damage Mechanics. Springer-Verlag, Berlin.

Melosh, H.J., Raefsky, A., 1980. The dynamical origin of subduction zone topography. Geophys. J. R. Astron. Soc. 60, 333–354.

Menéndez, B., Zhu, W., Wong, T.F., 1996. Micromechanics of brittle faulting and cataclastic flow in Berea sandstone. J. Struct. Geol. 18, 1–16.

Montési, L.G.J., Collins, G.C., 2005. On the mechanical origin of two-wavelength tectonics on Ganymede. Lunar Planet. Sci. XXXVI. Abstract 2093 .

Montési, L.G.J., Zuber, M.T., 2002. A unified description of localization for application to large-scale tectonics. J. Geophys. Res. 107. doi:10.1029/2001JB000465. B3, ECV 1–1.

Montési, L.G.J., Zuber, M.T., 2003. Spacing of faults at the scale of the lithosphere and localization instability: 1. Theory. J. Geophys. Res. 108. doi:10.1029/2002JB001923. B2, ETG 14–1.

Moresi, L., Mühlhaus, H.B., 2006. Anisotropic viscous models of large-deformation Mohr-Coulomb failure. Philos. Mag. 86, 3287–3305.

Mueller, S., McKinnon, W.B., 1988. Three-layered models of Ganymede and Callisto: Compositions, structures, and aspects of evolution. Icarus 76, 437–464.

Nanjo, K.Z., Turcotte, D.L., Shcherbakov, R., 2005. A model of damage mechanics for the deformation of the continental crust. J. Geophys. Res. 110, 7403. doi:10.1029/2004JB003438.

O'Neill, C., Nimmo, F., 2010. The role of episodic overturn in generating the surface geology and heat flow on Enceladus. Nat. Geol. 3, 88–91. doi:10.1038/ngeo731.

Owen, D.R.J., Hinton, E., 1980. Finite Elements in Plasticity: Theory and Practice. Pineridge Press Limited, Swansea, UK.

Pappalardo, R.T., Collins, G.C., 2005. Strained craters on Ganymede. J. Struct. Geol. 27, 827–838.

Pappalardo, R.T., Collins, G.C., Head, J.W., Helfenstein, P., McCord, T.B., Moore, J.M., Prockter, L.M., Schenk, P.M., Spencer, J.R., 2004. Geology of Ganymede. In: Bagenall, F., Dowling, T., McKinnon, W.B. (Eds.), Jupiter – The Planet, Satellites and Magnetosphere. Cambridge University Press, Cambridge, UK, pp. 363–396.

Pappalardo, R.T., and 15 colleagues, 1998. Grooved terrain on Ganymede: First results from Galileo high-resolution imaging. Icarus 135, 276–302, doi:10.1006/icar.1998.5966.

Patel, J.G., Pappalardo, R.T., Head, J.W., Collins, G.C., Hiesinger, H., Sun, J., 1999. Topographic wavelengths of Ganymede groove lanes from Fourier analysis of Galileo images. J. Geophys. Res. 104, 24057–24074. doi:10.1029/1998JE001021.

Patterson, G.W., Collins, G.C., Head, J.W., Pappalardo, R.T., Prockter, L.M., Lucchitta, B.K., Kay, J.P., 2010. Global geologic mapping of Ganymede. Icarus 207, 845–867. doi:10.1016/j.icarus.2009.11.035.

Petrenko, V.F., Whitworth, R.W., 1999. Physics of Ice. Oxford University Press, Oxford.

Poirier, J.P., 1980. Shear localization and shear instability in materials in the ductile field. J. Struct. Geol. 2, 135–142.

Poliakov, A.N.B., Buck, W.R., 1998. Mechanics of stretching elastic–plastic–viscous layers: Applications to slow-spreading mid-ocean ridges. In: Buck, W.R., Delaney, P.T., Karson, J.A., Lagabrielle, Y. (Eds.), Faulting and Magmatism at Mid-ocean Ridges. American Geophysical Union, Washington, DC, pp. 305–323.

Poliakov, A.N.B., Herrmann, H.J., 1994. Self-organized criticality of plastic shear bands in rocks. Geophys. Res. Lett. 21, 2143–2146. doi:10.1029/94GL02005.

Pollard, D.D., Fletcher, R.C., 2005. Fundamentals of Structural Geology. Cambridge University Press, New York.

Prockter, L.M., Patterson, G.W., 2009. Morphology and evolution of Europa's ridges and bands. In: Pappalardo, R.T., McKinnon, W.B., Khurana, K. (Eds.), Europa. University of Arizona Press, Tucson, pp. 237–258.

Ranalli, G., 1995. Rheology of the Earth, second ed. Chapman and Hall, London.

Regenauer-Lieb, K., Yuen, D.A., 2003. Modeling shear zones in geological and planetary sciences: Solid- and fluid-thermal–mechanical approaches. Earth Sci. Rev. 63, 295–349. doi:10.1016/S0012-8252(03)00038-2.

Rutter, E.H., Maddock, R.H., Hall, S.H., White, S.H., 1986. Comparative microstructures of natural and experimentally produced clay-bearing fault gouges. Pure Appl. Geophys. 124, 3–30. doi:10.1007/BF00875717.

Schenk, P.M., 2010. Atlas of the Galilean Satellites. Cambridge University Press, New York.

Schenk, P.M., McKinnon, W.B., Gwynn, D., Moore, J.M., 2001. Flooding of Ganymede's bright terrain by low-viscosity water–ice lavas. Nature 410, 57–60.

Schmalholz, S.M., Schmid, D.W., Fletcher, R.C., 2008. Evolution of pinch-and-swell structures in a power-law layer. J. Struct. Geol. 30, 649–663.

Showman, A.P., Stevenson, D.J., Malhotra, R., 1997. Coupled orbital and thermal evolution of Ganymede. Icarus 129, 367–383. doi:10.1006/icar.1997.5778.

Smith, B.A., and 21 colleagues, 1979a. The Galilean satellites and Jupiter: Voyager 2 imaging science results. Science 206, 927–950.

Smith, B.A., and 21 colleagues, 1979b. The Jupiter system through the eyes of Voyager 1. Science 204, 951–972.

Squyres, S.W., 1980. Volume changes in Ganymede and Callisto and the origin of grooved terrain. Geophys. Res. Lett. 7, 593–596.

Squyres, S.W., 1981. The topography of Ganymede's grooved terrain. Icarus 46, 156–168. doi:10.1016/0019-1035(81)90204-9.

Steele, J.M., 1989. Applied Finite Element Modeling: Practical Problem Solving for Engineers. M. Dekker, Inc., New York.

Tackley, P.J., 1998. Self-consistent generation of tectonic plates in three-dimensional mantle convection. Earth Planet. Sci. Lett. 157, 9–22.
Turcotte, D.L., Glasscoe, M.T., 2004. A damage model for the continuum rheology of the upper continental crust. Tectonophysics 383, 71–80.
Wang, C.Y., Mao, N.H., Wu, F.T., 1980. Mechanical properties of clays at high pressure. J. Geophys. Res. 85, 1462–1468.
Wijns, C., Weinberg, R., Gessner, K., Moresi, L., 2005. Mode of crustal extension determined by rheological layering. Earth Planet. Sci. Lett. 236, 120–134.
Wong, T.F., David, C., Zhu, W., 1997. The transition from brittle faulting to clastic flow in porous sandstone: Mechanical deformation. J. Geophys. Res. 102, 3009–3025.
Wu, F.T., 1978. Mineralogy and physical nature of clay gouge. Pure Appl. Geophys. 116, 655–689.
Yuen, D.A., Schubert, G., 1979. The role of shear heating in the dynamics of large ice masses. J. Glaciol. 24, 195–212.
Zahnle, K., Schenk, P., Levison, H.F., Dones, L., 2003. Cratering rates in the outer Solar System. Icarus 163, 263–289. doi:10.1016/s0019-1035(03)00048-4.
Zoback, M.D., Zoback, M.L., Eaton, J.P., Mount, V.S., Suppe, J., 1987. New evidence on the state of stress of the San Andreas fault system. Science 238, 1105–1111. doi:10.1126/science.238.4830.1105.
Zuber, M.T., Parmentier, E.M., 1996. Finite amplitude folding of a continuously viscosity-stratified lithosphere. J. Geophys. Res. 101, 5489–5498. doi:10.1029/95JB02514.